The radiative impact of out-of-cloud aerosol hygroscopic growth during the summer monsoon in southern West Africa

Sophie L. Haslett[1], Jonathan W. Taylor[1], Konrad Deetz[2], Bernhard Vogel[2], Karmen Babić[2],
Norbert Kalthoff[2], Andreas Wieser[2], Cheikh Dione[3], Fabienne Lohou[3], Joel Brito[4], Regis Dupuy[4],
Alfons Schwarzenboeck[4], and Hugh Coe[1]

[1]School of Earth and Environmental Sciences, University of Manchester, Manchester, United Kingdom
[2]Institute of Meteorology and Climate Research, Karlsruhe Institute of Technology (KIT), Karlsruhe, Germany
[3]Laboratoire d'Aérologie, Université Paul Sabatier Toulouse III (UPS), Toulouse, France
[4]Laboratoire de Météorologie Physique, Université Clermont Auvergne, Aubière, France

Correspondence to: Hugh Coe (hugh.coe@manchester.ac.uk)

Abstract.

Water in the atmosphere exists as both vapour and liquid water contained in particles. At high humidities, more water vapour condenses onto particles and causes them to swell, sometimes up to several times their original size. This significant change in size and chemical composition is termed hygroscopic growth and alters a particle's optical properties. Even in unsaturated conditions, this can change the aerosol direct effect, for example by increasing the extinction of incoming sunlight. This can have an impact on a region's energy balance and affect visibility. Here, aerosol and relative humidity measurements collected from aircraft and radiosondes during the Dynamics-Aerosol-Chemistry-Cloud Interactions in West Africa (DACCIWA) campaign were used to estimate the effect of highly humid layers of air on aerosol optical properties during the monsoon season in southern West Africa. The effects of hygroscopic growth in this region are of particular interest due to the regular occurrence of high humidity and the high levels of pollution in the region. The Zdanovskii, Stokes and Robinson (ZSR) mixing rule is used to estimate the hygroscopic growth of particles under different conditions based on chemical composition. These results are used to estimate the aerosol optical depth (AOD) for 63 relative humidity profiles. A static aerosol profile was assumed. Therefore, these results show the extent of the AOD frequency distribution that can be explained by humidity alone, rather than predicting actual AOD values. The median AOD in the region from these calculations was 0.46, which compares to a median of 0.36 measured by sun photometers. The shape of the AOD frequency distribution was largely comparable to that of the sun photometer measurements, demonstrating that relative humidity is able to account for a large part of the region's AOD variability. Humid layers are found to have the most significant impact on AOD when they reach relative humidities greater than 98 %, which can result in a wet AOD up to seven times larger than the dry AOD. Unsaturated humid layers were found to reach these high levels of relative humidity in 37 % of observed cases. Aerosol concentrations in southern West Africa are projected to increase substantially in the coming years; results presented here show that the presence of highly humid layers in the region is likely to enhance the consequent effect on AOD significantly.

1 Introduction

Aerosol particles can absorb water even in sub-saturated conditions. In humid environments, this process can increase their size substantially. This increase in the aerosol liquid water content affects a particle's interactions with radiation by increasing its diameter and changing its refractive index. Therefore, increased aerosol water content can alter the aerosol direct effect on radiative forcing. In addition, these alterations to aerosol characteristics can affect visibility and form haze or alter the chemical interactions of particles in the atmosphere (Chen et al., 2012).

The extent to which an aerosol particle takes on water (its hygroscopic growth) is dependent on a number of variables, including its chemical composition and the relative humidity (RH) in its environment. Due to the complexity of this function, hygroscopic growth has been identified as one of the key uncertainties in aerosol radiative forcing (Forster et al., 2007). While the growth of inorganic aerosol species is reasonably well understood, the complexity of organic aerosols, which can include hundreds of different compounds, has made it difficult to establish a definitive approach to investigating its hygroscopic properties in a mechanistic way (Gysel et al., 2007; Topping et al., 2005). A number of studies have been carried out, to examine hygroscopic growth empirically in the ambient environment (Esteve et al., 2014; Gysel et al., 2007; Hersey et al., 2009; Highwood et al., 2012; Kamilli et al., 2014; Liu et al., 2011).

A particle's hygroscopic properties can be described using kappa (κ), which was developed by Petters and Kreidenweis (2007) to collate all of the chemical variables that affect hygroscopicity into a single parameter. Although this value can vary slightly with RH and temperature, it is robust enough to be considered a constant for a given chemical composition in most ambient cases. This value is closely related to an aerosol's hygroscopic growth factor (HGF) in a given environment - the ratio between its diameter after it has absorbed water and its dry diameter. These quantities present challenges for measurement, as the majority of aerosol instruments dry aerosol particles before measuring their properties.

Some studies have used the Hygroscopic Tandem Differential Mobility Analyser (H-TDMA) to measure the wet diameters of aerosol particles (Swietlicki et al., 2008), which makes a direct calculation of the HGF possible above relative humidities of around 90 %. A particle's hygroscopicity depends on its chemical constituents. Therefore, another approach is to estimate aerosol water content based purely on measurements of chemical composition and on an aerosol population's size distribution. If an aerosol population with different chemical constituents can be assumed to be internally mixed, the Zdanovskii, Stokes and Robinson (ZSR) mixing rule (Stokes and Robinson, 1966; Zdanovskii, 1948) allows the HGF of a mixed particle to be estimated based on the known growth factors of the pure constituents. While ambient aerosol is known to exist in a combination of internal and external mixing states, this assumption is reasonable for more aged, regional aerosol populations (Boucher et al., 2013; Pratt and Prather, 2010). When the HGF is known, the size distributions and known densities of aerosol particles and consituents can be used to estimate the volume of water in an aerosol sample. A number of closure studies have been carried out to assess the reliability of these calculations compared with H-TDMA measurements, with compelling results

(Gysel et al., 2007; Hersey et al., 2009; McFiggans et al., 2005). Both McFiggans et al. (2005) and Gysel et al. (2007) found closure was not possible when nitrate loadings were included in calculations. However, Gysel et al. (2007) suggested that this was likely due to the evaporation of nitrate in the H-TDMA. As such, ZSR calculations are likely more reliable than direct measurements of HGF for nitrate-containing particles.

60

A number of recurring features have been observed in various HGF measurements: Aklilu et al. (2006) noted that a high proportion of sulphate is often correlated with high HGF values. This is related to the highly hygroscopic nature of sulphate-containing aerosols compared with other species. Studies have shown that organic aerosol does grow hygroscopically, though to a lesser extent than many inorganic species. The HGF is slightly larger for secondary organics and more aged aerosol due to its high oxidation levelsl However, the influence of even highly-oxidised organic compounds is small compared with that of inorganic compounds. Therefore, the organic to inorganic ratio has been found to be a more influential factor for the HGF than the composition of the organic aerosol itself (McFiggans et al., 2005). A single value is therefore often used to represent the HGF of organic aerosol. Urban environments have been found to include several types of aerosol that are primarily hydrophobic (they do not readily absorb water). These include freshly emitted combustion particles due to their high soot content, and insoluble organic compounds (Swietlicki et al., 2008). The HGF correlates closely with the RH in a region, and has been found to follow diurnal patterns in RH closely (e.g. Liu et al., 2011).

When the aerosol water content in a region has been calculated, this value can be used in tandem with the calculated refractive index of wet particles to calculate changes to the scattering and extinction properties of the particles, for example using a framework like that described by Esteve et al. (2014). Thus, changes to the radiative properties of particles and their consequent impact on radiative forcing can be estimated.

During the monsoon season in West Africa, the RH is often high, which results in substantial aerosol hygroscopic growth. Therefore, this is a region in which hygroscopic growth is likely to have a large impact on radiative forcing. This supposition is supported by a previous study in southern West Africa, which found a strong increase in backscatter in the region between 18:00 and 00:00 UTC. This was thought to be related to aerosol growth due to increases in humidity during these times (Babić et al., in press). Anthropogenic emissions in the region are projected to increase substantially by 2030 (Liousse et al., 2014), which will increase the impact of this hygroscopic growth.

This study presents radiosonde and aircraft data from the Dynamics-Aerosol-Chemistry-Cloud Interactions in West Africa (DACCIWA) campaign, a large field campaign that took place in southern West Africa during June and July 2016 (Knippertz et al., 2015, 2017; Flamant et al., 2018a). Chemical and physical aerosol measurements from the British Antarctic Survey (BAS) Twin Otter and the French Service des Avions Français Instrumentés pour la Recherche en Environnement (SAFIRE) ATR-42 aircraft are presented here. The ZSR technique has been used to estimate the HGF and aerosol liquid water content

90 based on chemical measurements.

2   Data and Methods

Data were obtained during the DACCIWA aircraft and ground-based campaigns in southern West Africa during June and July

2016 (Flamant et al., 2018a; Kalthoff et al., 2018). The data presented here were collected by the British Antarctic Survey Twin

95 Otter aircraft, from 11 flights carried out between 6 July and 15 July. The Twin Otter's operating area during the campaign

was from 0.6 °W to 2.7 °E and from 5.4 °N to 8.0 °N. During DACCIWA, airborne measurements were made of aerosol

properties with a focus on both regional aerosol properties and the effects of urban emissions. Flight patterns consisted of a

series of profiles, and straight and level runs at different altitudes. The focus of the Twin Otter aircraft was on low-tropospheric

measurements, below 3 km. Instrumentation on board the aircraft measured submicron aerosol chemical composition, optical

100 properties and physical properties.

An Aerodyne Compact Time-of-Flight Aerosol Mass Spectrometer (AMS) (Aerodyne Research Inc., Billerica, MA, USA)

(Canagaratna et al., 2007; Drewnick et al., 2005) was used to measure the chemical composition of the submicron non-

refractory aerosol mass. Measurements of organics, nitrate, sulphate and ammonium were collected; chloride concentrations

105 were found to be consistently below the instrument's detection limit and so are not included here. The ionisation efficiency of

the instrument was calibrated several times during the campaign using ammonium nitrate and once with ammonium sulphate.

A collection efficiency of 0.5 was applied to the data, which is typical for ambient data (Middlebrook et al., 2011). Compar-

isons between the AMS and the volume convolved size distribution show that other components, for example mineral dust,

contribute little to the submicron aerosol mass and that coarse mode concentrations were low. Black carbon concentrations

110 were established using a Single Particle Soot Photometer (SP2) (Droplet Measurement Technologies, Longmont, CO, USA).

This produced a time series of the mass concentration of refractory black carbon larger than $0.3\,\mathrm{fg}$. Calibrations using Aquadag

were carried out several times during the campaign, with the standard correction of 0.75 applied (Laborde et al., 2012). Particle

size distributions were measured by a TSI Scanning Mobility Particle Sizer (SMPS) on board the ATR-42 aircraft. This aircraft

carried out DACCIWA flights during the same time period as the Twin Otter, including a significant number in the region of

115 interest here (Brito et al., 2018). The SMPS determines particle sizes using electrical mobility, scanning through the size range

from 0.02 - 0.5 μm. This produces an aerosol size distribution every 120 s.

Observations were considered alongside RH profiles from a number of radiosonde soundings from the DACCIWA supersite

in Savè. Radiosonde releases were carried out from the Savè supersite for a period of two months (June and July), with several

120 releases being made each day. This allowed the compilation of a robust set of RH statistics. The setup of measurements and the

overview of the diurnal cycle of the atmospheric boundary layer conditions from the Savè ground site are presented in more
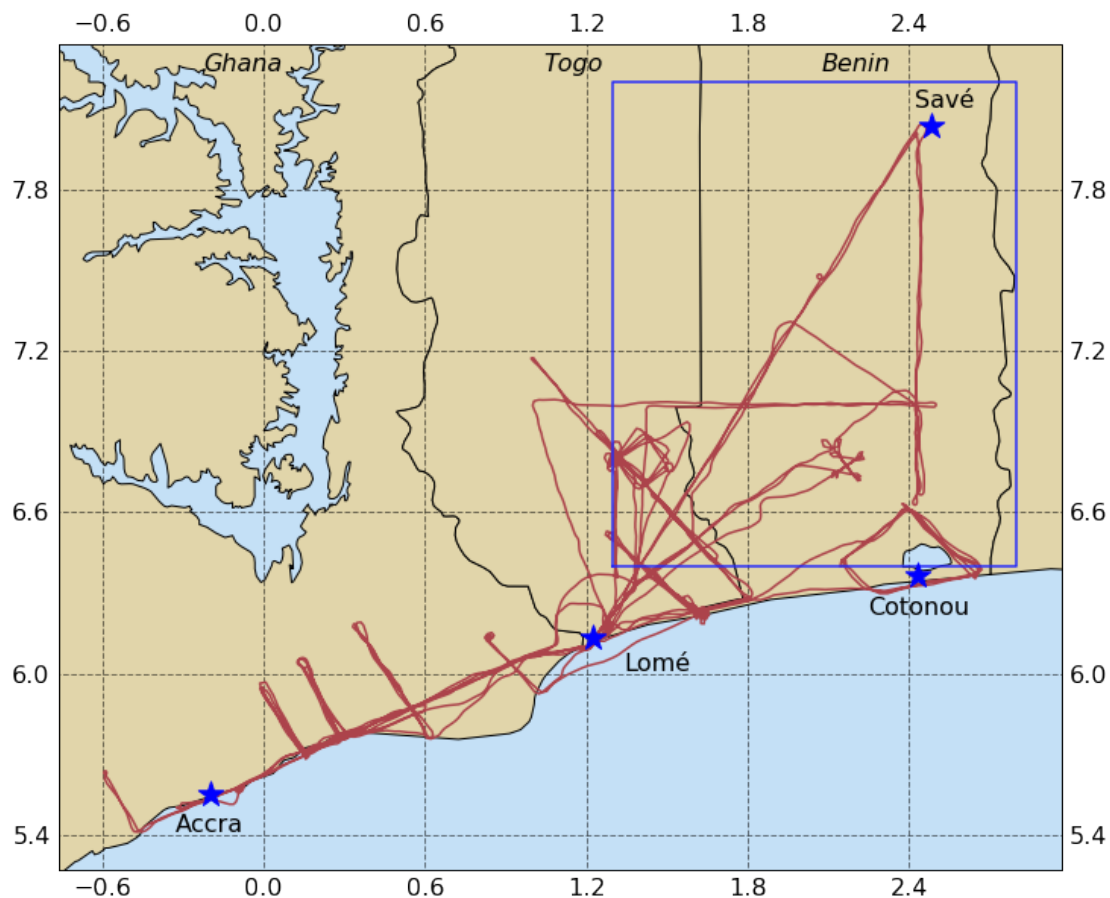
Figure 1. Map of the Twin Otter flight paths. The blue box represents locations where data was used in this analysis to compare with radiosonde data from the Savè supersite.

detail by Kalthoff et al. (2018).

In order to ensure that aircraft data were comparable with RH readings in this region, aircraft data have been included here if
125   collected further north than 6.4 °N and further east than 1.3 °E. The chemical aerosol data collected in this region were found
to be reasonably invariant across the campaign period (medians and interquartile ranges are displayed in Fig. 2); thus, these
data have been averaged in order to increase the robustness of results. As observations of RH were taken from the Savè ground
site, results shown here apply to the atmosphere above Savè. The Twin Otter flight tracks from the campaign are displayed in
Fig. 1.

2.1 κ-Köhler theory and the ZSR mixing rule

The single-parameter approach to describing a particle's propensity to grow hygroscopically proposed by Petters and Kreidenweis (2007) was employed here. This combines all variables that depend on a particle's chemical composition into a single parameter, κ. The relationship between the κ-value and the HGF is expressed by Eq. 1:

$$\frac{RH}{exp(\frac{A}{D_d HGF})} = \frac{HGF^3 - 1}{HGF^3 - (1-\kappa)} \tag{1}$$

where RH is the relative humidity expressed as a fraction, HGF is the hygroscopic growth factor, D_d is the dry particle diameter and

$$A = \frac{4\sigma_{s/a} M_w}{RT\rho_w} \tag{2}$$

where $\sigma_{s/a}$ is the surface tension at the solution-air interface, M_w is the molar mass of water, R is the universal gas constant, T is the absolute temperature and ρ_w is the density of water. This equation is solved iteratively.

The value of κ increases with increasing hygroscopicity. Thus, κ will be 0 for a non-hygroscopic particle and above 1 for the most hygroscopic particles. Typically, values for continental ambient aerosol fall between 0.1 and 0.4 (Pringle et al., 2010). Values of κ used for the species considered here are listed in table 1. If ambient aerosol is assumed to be internally mixed, the κ values of the different components can be combined to provide a total κ value for the mixed particle, using Eq. 3:

$$\kappa = \sum_i \varepsilon_i \kappa_i, \tag{3}$$

where ε_i represents the volume fraction of an individual chemical component. This follows from the ZSR mixing rule described by Zdanovskii (1948) and Stokes and Robinson (1966). Once the value of κ has been determined for a given particle and if the RH is known, the relationship shown in Eq. 1 can be used to calculate the particle's expected HGF.

2.2 Ion pairing

The AMS provides a time series of nitrate (NO_3^-), sulphate (SO_4^{2-}) and ammonium (NH_4^+) fragments. However, quantities of complete neutral salts are needed in order for the ZSR mixing rule described above to be used. Here, moles of neutral salts were established using the ion pairing scheme outlined by Gysel et al. (2007), as shown in Eq. 4. Calculations for H_2SO_4 and

Table 1. Density, kappa values and refractive indices for aerosol species considered here.

Species	Density ($\mathrm{kg\,m^{-3}}$)	κ	Refractive index
NH_4NO_3	1725^a	0.68^f	$1.6 - 0i^a$
$(NH_4)_2SO_4$	1769^b	0.52^f	$1.53 - 0i^i$
NH_4HSO_4	1780^c	0.56^f	$1.47 - 0i^c$
Organics	1200^d	0.1^g	$1.46 - 0.021i^d$
Black carbon	1800^e	0^h	$1.85 - 0.79i^j$

[a] Weast (1985), in Morgan et al. (2010)

[b] Penner et al. (1998), in Morgan et al. (2010)

[c] Lowenthal et al. (2003)

[d] Stelson (1990), in Taylor et al. (2015)

[e] Bond and Bergstrom (2006), in Morgan et al. (2010)

[f] Liu et al. (2014)

[g] Suda et al. (2012)

[h] Weingartner et al. (1997), in Jurán, i et al. (2010)

[i] Toon et al. (1976), in Morgan et al. (2010)

[j] Bond and Bergstrom (2006)

HNO_3 are not included as the aerosol was found to be acidically neutral in all cases considered here.

$$n_{\mathrm{NH_4NO_3}} = n_{\mathrm{NO_3^-}}$$

$$n_{\mathrm{NH_4NSO_4}} = min(2n_{\mathrm{SO_4^{2-}}} - n_{\mathrm{NH_4^+}} + n_{\mathrm{NO_3^-}}, n_{\mathrm{NH_4^+}} - n_{\mathrm{NO_3^-}}) \tag{4}$$

$$n_{\mathrm{(NH_4)_2SO_4}} = max(n_{\mathrm{NH_4^+}} - n_{\mathrm{NO_3^-}} - n_{\mathrm{SO_4^{2-}}}, 0)$$

2.3 Optical properties

Aerosol optical properties were calculated using Mie code, based on a set of algorithms developed by Yang (2003), which uses a supplied refractive index, wavelength of light and aerosol diameter to calculate properties including the extinction coefficient for a multi-layered sphere. The refractive index used here was calculated by considering the weighted sum of the refractive indices of the individual chemical compounds in a particle, again assuming volume mixing. This technique does not account for some effects, including possible lensing effects from the addition of water to particles or the co-condensation of other volatile compounds with water. The individual refractive indices of the components considered are shown in table 1. The effect of absorbed water on the refractive indices was taken into account, with the refractive index for water of $1.33 - 0i$ being used.
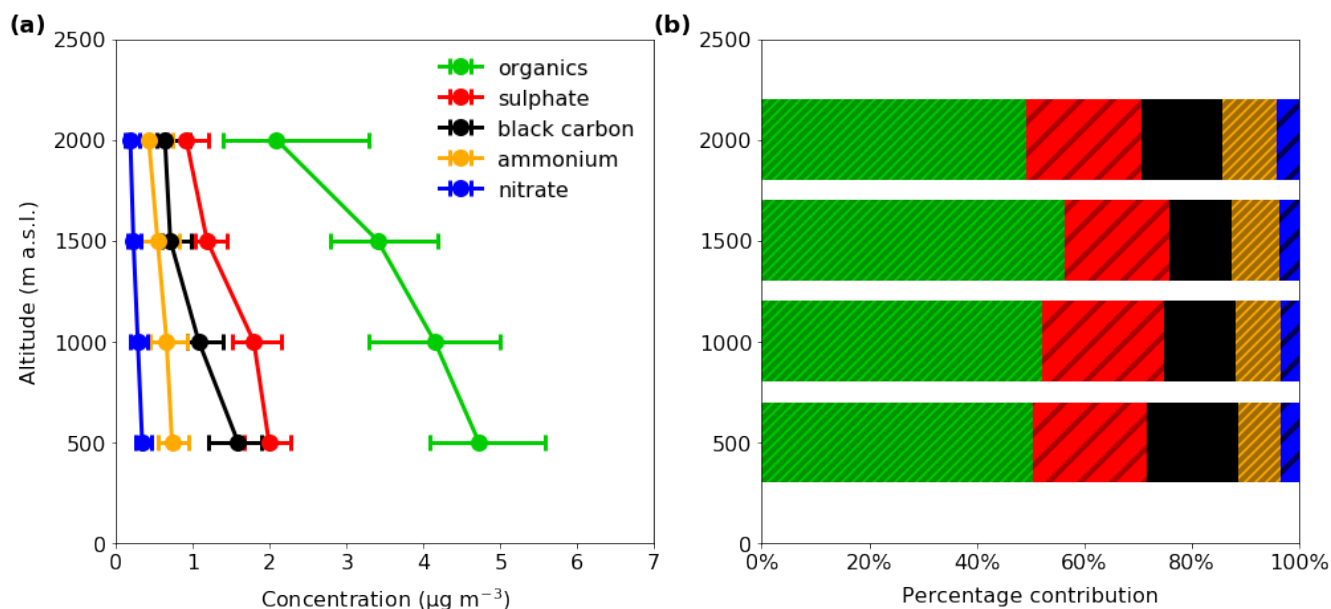
Figure 2. **(a)** Average chemical composition of aerosol in the Savè region, as measured by the AMS. Results are displayed at standard temperature and pressure (STP) and altitude is above sea level (a.s.l.) The centre point indicates the median concentration and the bars the lower and upper quartiles. **(b)** The percentage contribution of each chemical species in each altitude bin.

3   Results

Figure 2a shows the average chemical composition of submicron aerosol in the region outlined by the box in Fig. 1. Data have been averaged to four bins at altitudes of 500 m, 1000 m, 1500 m and 2000 m. Figure 2b shows the relative proportions of each

170   chemical species at each of these four altitudes. As can be seen, the chemical distribution of aerosol was reasonably stable in this region, with the overall concentration decreasing with altitude. Organic aerosol contributed the largest proportion to the aerosol loading, making up over 50 % of the total mass. SO_4^{2-} contributed around 20 % in all cases. Black carbon was just under 15 %. Contributions from NO_3^- and NH_4^+ were each less than 10 %.

175   The aircraft measurements carried out in the target area were insufficient to determine a diurnal cycle in aerosol loading. Therefore, the aerosol concentration and distribution is assumed here to remain constant throughout the day. Given the relative stability of the distribution between different chemical species at different altitudes within the lowest 2 km, this distribution is assumed here to be the same in all locations. The composition used was 52 % organic, 21 % sulphate, 14 % black carbon, 9 % ammonium and 4 % nitrate, which was established by averaging the distributions across the four altitude bins. The value of κ

180   for this composition was calculated using the method described in Section 2.1, assuming the composition to be the same across the size distribution. This produced a value of $\kappa = 0.22$, which is typical for ambient aerosol (Pringle et al., 2010).

Figure 3 shows the normalised average number and volume size distributions of submicron aerosol in the region outlined by the blue box in Fig. 1, as measured by the SMPS on board the ATR aircraft. Two distinct size modes can be seen at most

185 heights, indicating that the region contains smaller, fresher aerosol with a mode at around 60 nm; and a large, accumulation mode containing more aged aerosol. The volume size distribution showed that the majority of the aerosol volume, and therefore the majority of the mass, was in the accumulation mode.

Figure 4 shows RH measurements from radiosondes released from the ground site in Savè. These plots show the mean RH

190 and standard deviations at every 100 m interval up to 3 km, averaged across four times of day. These data show a clear diurnal cycle in the RH, with a humid boundary layer during the night and early morning becoming drier towards noon and into the evening. These features are characteristic of the Gulf of Guinea maritime inflow (Adler et al., 2017; Deetz et al., 2018b), a coastal air mass that propagates inland in the evening, bringing cool air to the southern West African region. The increase of RH in the evening is mainly caused by cooling due to this cold air advection (Adler et al., in press; Babić et al., in press).

195 The RH in the pre-frontal region is generally around 75 %, while post-frontal RH rises to be almost consistently above 90 % (Deetz et al., 2018a) and leads to low-level cloud formation in the night (Adler et al., in press; Babić et al., in press).

The dataset of RH measurements used here is valuable, as models are often unable to replicate the vertical RH profile (Hannak et al., 2017). This is due to the complex interplay between shallow and deep convection, which changes the vertical

200 distribution of water vapour and clouds. These factors influence the surface energy budget, which can in turn create deep convection, in a feedback loop. The uptake of water by aerosol particles adds another layer of complexity to this picture.

The time series panel gives insight into the day-to-day variability in RH. Four phases of the 2016 West African monsoon have been defined by Knippertz et al. (2017) and are delineated by the vertical dashed lines in Fig. 4e. The first, pre-onset

205 phase was characterised by rainfall near the coast, which moved inland during the second, post-onset phase. This can be seen in the drier start to the period shown in Fig. 4e. This was followed by a period of higher humidity in phase 2, during which humidities rarely dropped below 80 %. The final week of the post-onset phase was slightly drier than those preceding it, which was associated with a cyclonic system that passed Savè on 16 July, transporting dry air northwards (Kalthoff et al., 2018). During phase 3, the rainfall maximum shifted again back to the coast and during phase 4, the recovery of the monsoon, the

210 maximum was once again found inland.

Using an average aerosol particle size of 200 nm (as measured by the SMPS) and assuming a constant aerosol composition throughout the day, it was possible to estimate the average HGF of particles at each of the altitudes and times of day in Fig. 4 using the method described in sections 2.1 and 2.2. These results are displayed in Fig. 5. The plots show the extent to which

215 the diameter of an average particle would be expected to grow under the given conditions. The shape of the HGF profiles is governed by the RH statistics shown in Fig. 4. It can be seen that the sensitivity to changes in RH is more pronounced where the humidity is high. In drier regions, for example at low altitudes at 18 UTC, reasonably significant variation in RH produces
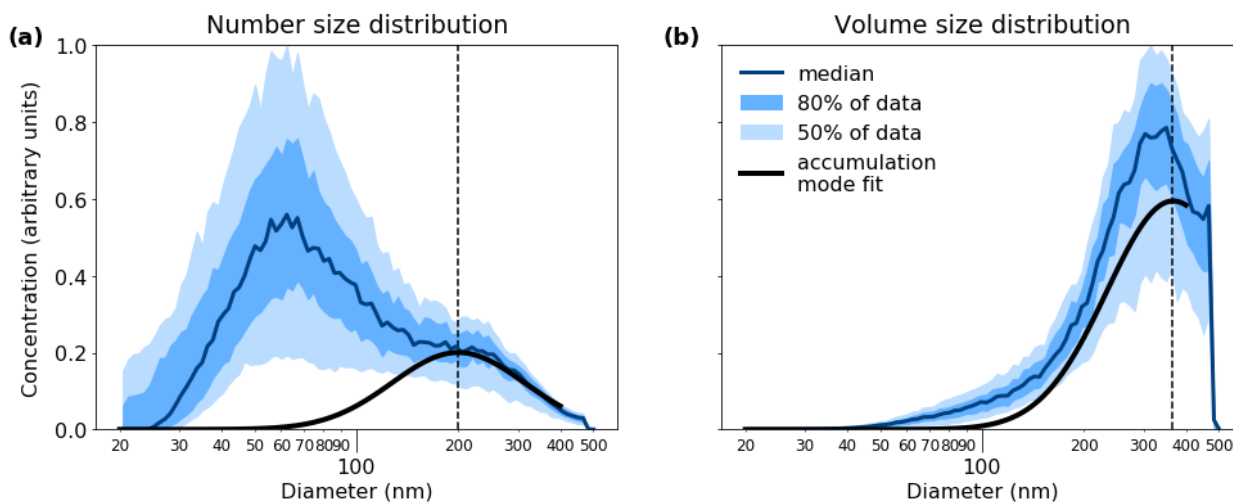
Figure 3. The **(a)** number size distribution and **(b)** volume size distribution of submicron aerosol below 2500 m in the area outlined by the box in Fig. 1. The dark blue lines show the median size distributions; the darker shading represents data between the 25th and 75th percentiles (50 % of the data) and the lighter shading data between the 10th and 90th percentiles (80 % of the data). The thick black line represents a lognormal curve fitted to the accumulation mode.

very little change in particles' hygroscopic growth. This suggests that even thin layers of high RH are likely to have a dispro-
portionately large impact on the radiative properties of the column. The particles are larger due to the high RH, and these larger
220 particles scatter sunlight more effectively.

Ceilometer observations from the DACCIWA ground site in Savè during the campaign have been explored by (Babić et al., in press).
This instrument uses a laser to determine atmospheric backscatter, which allows the determination of cloud base. A strong in-
crease in backscatter was noted between 18:00 and 00:00 UTC, which is thought to be related to aerosol hygroscopic growth.
225 The frequently high HGF layers shown here are consistent with this interpretation.

The volume of absorbed water at high humidities can make a significant difference to the composition and properties of
aerosol particles. Figure 6a shows the percentage contribution of the compounds being considered here to the particle volume
at different relative humidities. Above around 80 % RH, water contributes over half of the volume and above around 95 % RH,
230 water contributes more than 80 % to the volume of an individual particle, both growing the particle substantially and changing
its optical properties. The decrease in aerosol refractive index as the particles grow is illustrated in Fig. 6b.
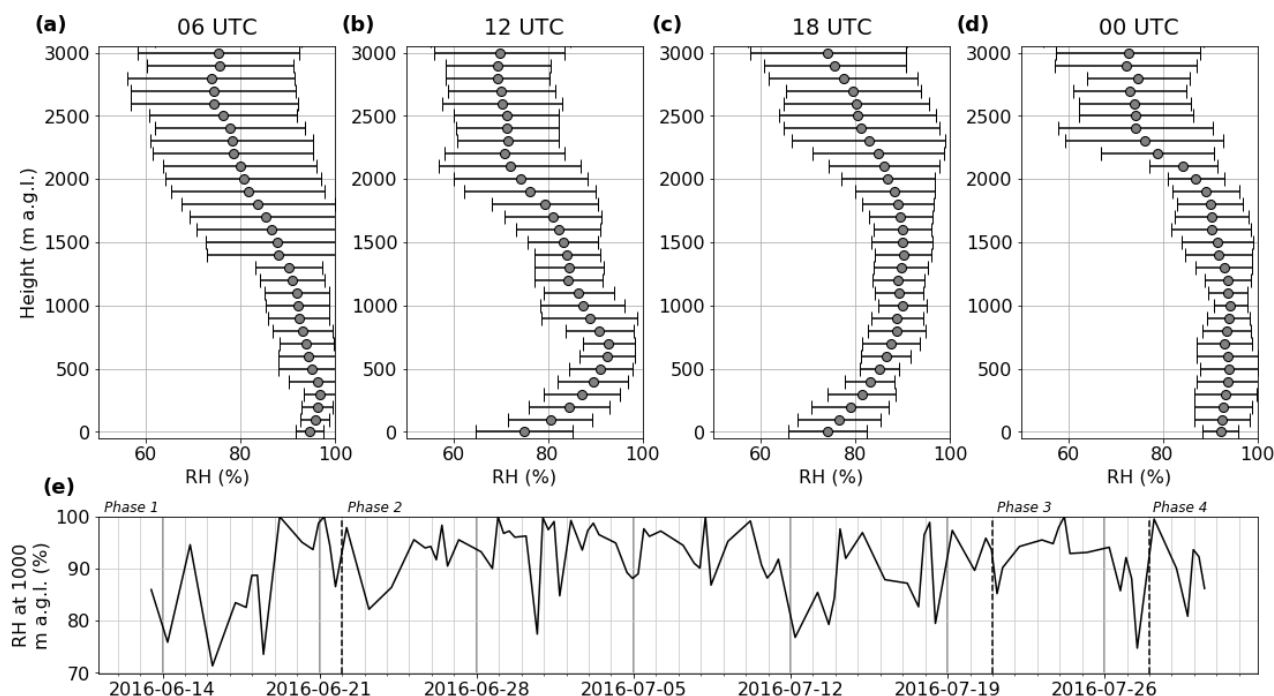
Figure 4. The mean and standard deviation of relative humidity measurements with altitude at **(a)** 06 UTC (n=46), **(b)** 12 UTC (n=15), **(c)** 18 UTC (n=20) and **(d)** 00 UTC (n=15), from radiosondes launched from the Savè ground site. Altitudes are above ground level (a.g.l.) **(e)** A time series of the RH at 1000 m. Dashed vertical lines indicate the four different monsoon phases, as defined by Knippertz et al. (2017). (NB: Local time in Benin is UTC+1hr.)

3.1 Calculating aerosol optical depths

In order to establish the impact of humid layers on column optical properties, the sub-3 km aerosol optical depth (AOD) was
235 calculated for each of the 63 unsaturated radiosonde profiles taken from the Savè ground site during the DACCIWA campaign. The steps of the approach used to establish the AOD are outlined below using a case study RH profile from 8 July at 1057 UTC (local time = UTC). This approach was then applied to all RH profiles in the dataset.

1. Find a representative mass concentration profile.

240 A number of aircraft profiles were carried out in the region of interest during DACCIWA. However, several of these intercepted cloud during the profile, covered only a small altitude span or did not have all necessary instruments functioning. A single profile was therefore chosen to represent the average aerosol loading in all cases. The chosen profile took place on 8 July at 1057 UTC at 7.31 °N, 1.98 °E: about two thirds of the way along the line from Lomé to Savè. This profile did not intercept cloud and spanned from 500 m to 2500 m. The concentrations observed were close to the
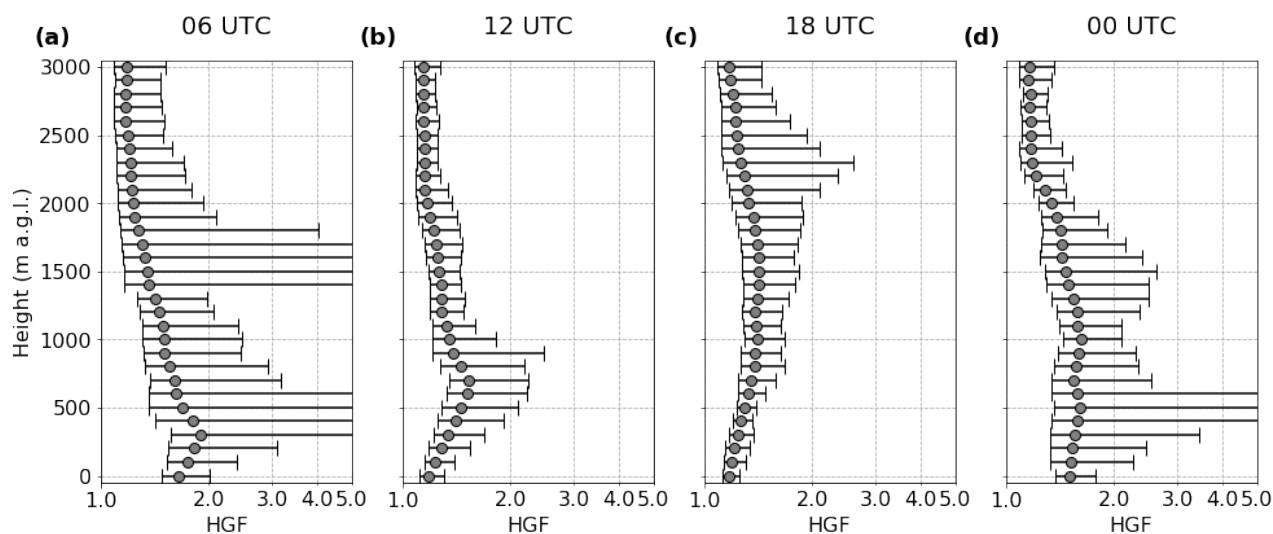
Figure 5. The mean and standard deviation of estimated hygroscopic growth factors at **(a)** 06 UTC, **(b)** 12 UTC, **(c)** 18 UTC and **(d)** 00 UTC. Where the upper value cannot be seen, this is where the air became saturated.
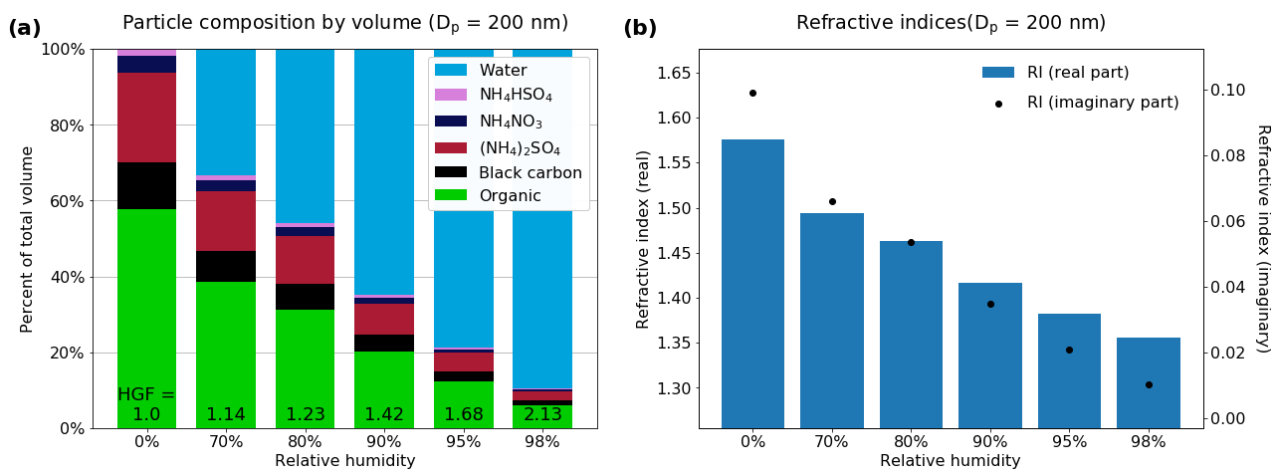
Figure 6. (a) The fractional composition of 200 nm particles at different relative humidities and **(b)** the effect of the additional water volume on the particle's refractive index. These values have been calculated using the ZSR mixing rule.
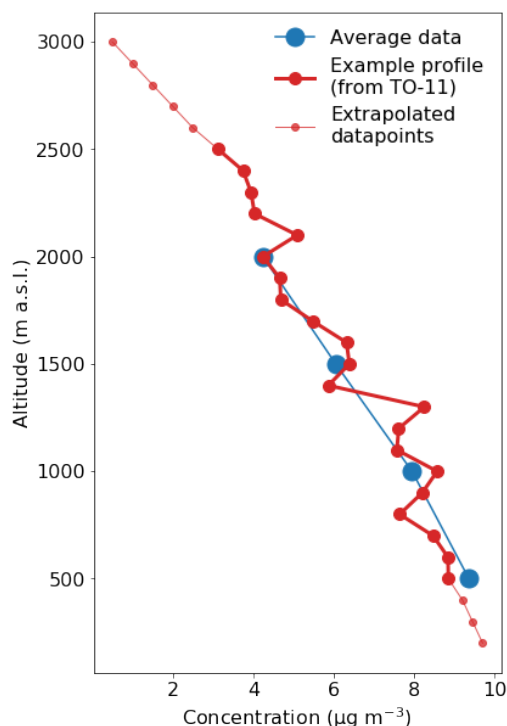
Figure 7. The average mass concentration profile across the campaign (blue) and the representative profile chosen from 8 July. Small markers at the top and bottom of the profile are extrapolated values.

average profile, making it illustrative of aerosol mass concentrations in the region as a whole. The shape of the aerosol profile was extrapolated above 2500 m and below 500 m, assuming the continuation of a roughly similar gradient, as shown in Fig. 7. This single representative profile was used to calculate the AOD for all of the radiosonde profiles. Aerosol variation is not taken into account here as the aim of this study is to explore the extent of the effect of humid layers on aerosol optical properties.

2. Establish an idealised aerosol size distribution at each altitude.

Figure 3 shows the average aerosol size distribution at different altitudes, with two clear modes (Aitken and accumulation mode) being identified. In terms of aerosol hygroscopicity and changes to optical properties, the larger mode is the most significant as it contains the vast majority of the aerosol volume and is of a size comparable with incoming radiation, making it the more optically active size range. The number distribution is dominated by the small, fresh Aitken mode aerosol, which shows a large degree of variation but contributes little to the overall optical properties of the aerosol; therefore, the accumulation mode was isolated here to calculate optical effects. It can be noted from Fig. 3 that there is little variation in the size and shape of the accumulation mode across different altitudes. The aerosol frequencies at different diameters generally fall within around 40 % of one another. This strongly suggests that a reasonably consistent
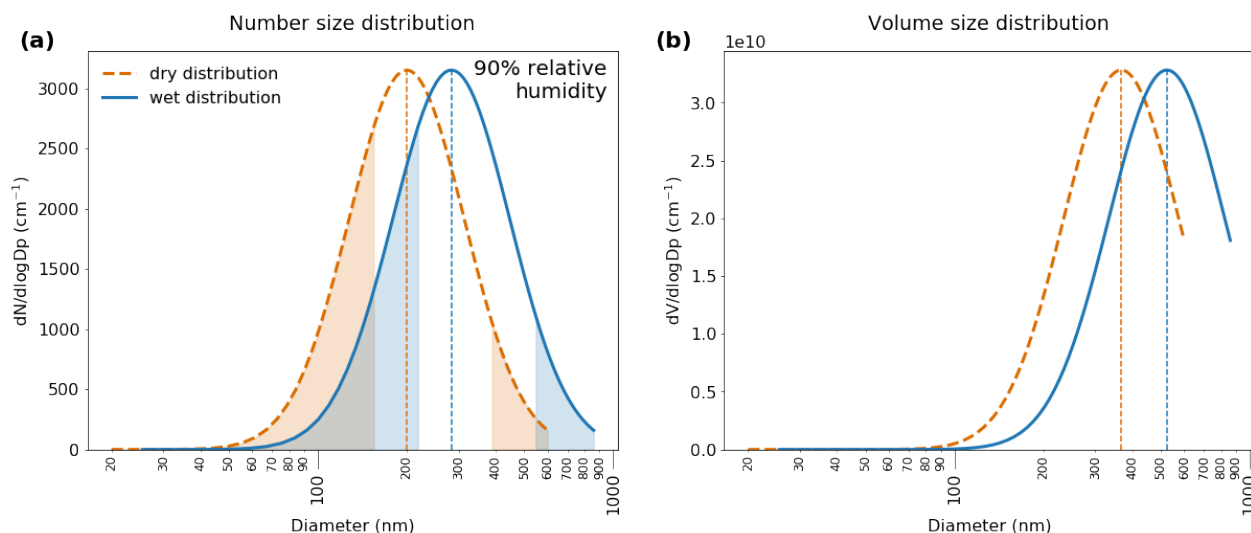
Figure 8. The dry and wet idealised **(a)** number and **(b)** volume size distributions based on an aerosol mass of $10\,\mu g\,m^{-3}$ and an RH of 90 %.

accumulation mode can be expected, which will likely scale with the overall aerosol mass.

260

The thick black lines in Fig. 3 show lognormal distributions that have been fitted to the accumulation mode. The mode is at 200 nm. The shape and mode of the distribution were assumed to remain constant across all altitude bins and the amplitude was adjusted according to the assumed aerosol mass at a given altitude. This produced an idealised accumulation mode size distribution of the same shape, but differing amplitudes at each altitude.

265

3. Grow the wet aerosol size distribution.

At each altitude bin, HGFs were used to 'grow' the dry size distribution. An HGF was established and applied to each bin in the idealised dry size distribution, which allowed the shape of the new, wet size distribution to be calculated. An example can be seen in Fig. 8 for an idealised dry size distribution based on an aerosol mass of $10\,\mu g\,m^{-3}$, assuming an

270 RH of 90 %.

4. Calculate AOD.

The chemical distribution, including water, of aerosol particles in each bin of the wet size distribution was used to calculate particles' refractive indices. Their extinction coefficients were then calculated using Mie code. The total extinction

275 coefficient in Mm^{-1} at each altitude was determined by integrating these across the whole wet size distribution. This provides a quantification of the extent to which incoming radiation would be attenuated at each altitude. Integrating these with altitude gives the AOD of the column. In Fig. 9, the total AOD for the example radiosonde RH profile and
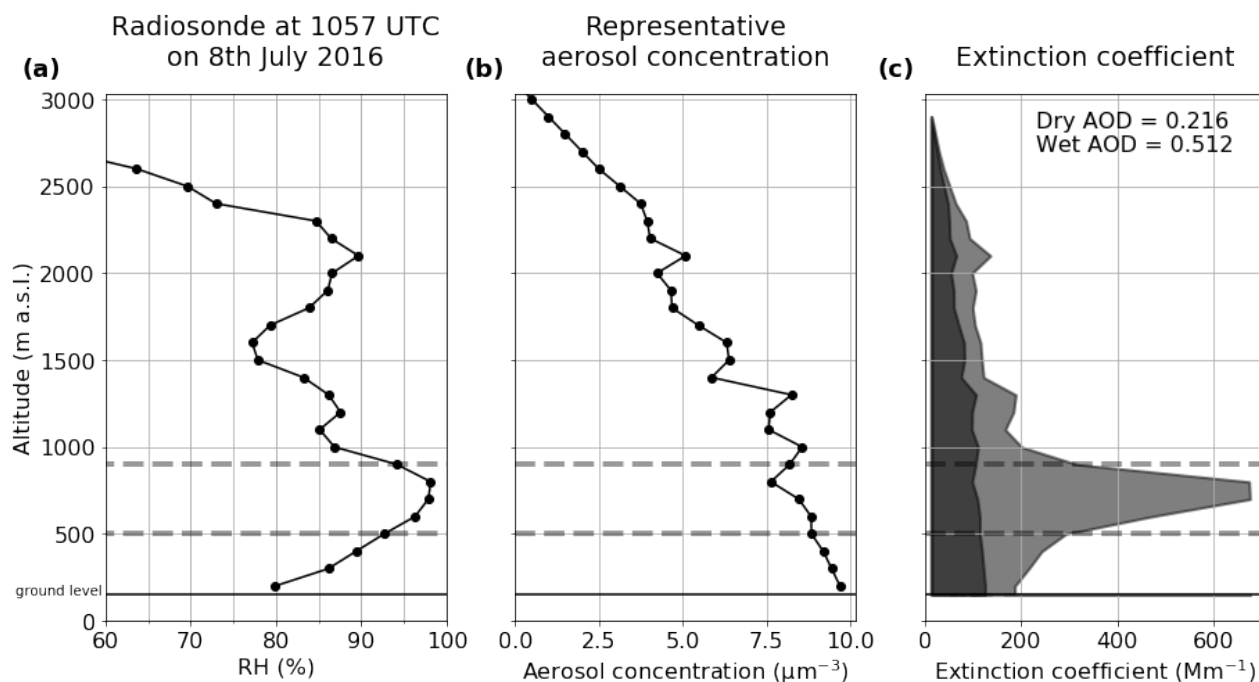
Figure 9. The **(a)** relative humidity and **(b)** aerosol concentrations used to calculate AOD, and **(c)** the profile of dry and wet calculated extinction coefficients for the case study RH profile example on 8 July. The solid black line shows ground level at Savè. The dashed grey lines outline the humid layer with RH greater than 95 %. In the third panel, the darker filled shape shows the dry extinction coefficient in the column and the lighter filled shape shows the wet extinction coefficient.

the representative aerosol concentration are shown along with a profile of the dry and wet extinction coefficients at each altitude. The total AOD of the wet profile is more than double that of the dry profile.

280

This example shows the disproportionate contribution towards AOD from layers of high humidity, such as that highlighted in grey in this example. Although the wet extinction coefficients are higher than the dry ones at every altitude, this effect is exaggerated in this humid layer. The region highlighted in grey contributes over 35 % to the total AOD, despite representing less than 20 % of the column height.

285 The approach outlined above has been used to calculate the AOD for all 63 unsaturated radiosonde RH profiles collected from Savè. Fig. 10 shows a frequency plot of these calculated AODs, which are coloured according to the time of day the sonde was released (+/- one hour). These values are calculated purely based on variations in RH. The frequency distribution therefore quantifies an estimate of the variation in AOD due entirely to RH; it does not show a true estimate of AOD for each profile, which would require a larger number of varying parameters. This plot is shown alongside a frequency distribution of 290 the AODs measured by sun photometer from the Savè ground site. The sun photometer dataset includes 319 measurements

taken between 8 June and 29 July 2016 as part of the DACCIWA field campaign.

There is good general agreement between the AOD values calculated here and those collected by sun photometer over a similar period. The modal AOD in both datasets falls between around 0.3 and 0.4. Values of AOD in the early morning were often higher than those in the middle of the day or the evening. The minimum value in the sun photometer dataset was a little less than 0.2, while that of the calculated dataset was closer to 0.3. This likely represents days with low aerosol loadings, which are not captured by the model applied here to the calculated dataset as it assumes a constant aerosol profile. Both datasets, however, show a high tail. The bulk of the datapoints in both cases are lower than 0.8. The calculated AOD dataset has a number of higher values, which are not seen in the measured dataset. These cases are likely to occur at times of very high RH, when broken clouds were likely present. Given that sun photometer measurements are not carried out when there is cloud cover, which is determined using an algorithm, it is likely that such measurements were simply not carried out at times that would correspond to these high calculated AOD values. The calculated dataset is based solely on observations in the lowest 3 km. As such, any high-level aerosol layers are not taken into account.

It is important to note that the calculated values here are not expected to reproduce the real-world AOD for any given RH profile. A number of values are assumed to be constant here, including the shape and magnitude of the aerosol profile, the aerosol chemical composition and the shape of the accumulation mode size distribution. Although it can be shown that the variability in these values was low, a realistic calculation would require variation in such quantities to be taken into account. This dataset, instead, gives an estimate of the variability in the AOD measurements that is due entirely to changes in RH. Despite this limitation, this approach is able to replicate a large part of the measured AOD frequency distribution. This strongly suggests that the majority of the variation in the AOD observations in this region is related to variations in RH.

3.2 The effect of high humidity layers on AOD

In the example case study shown in Fig. 9, the humid layer between 600 m and 900 m had a significant effect on the calculated column AOD. In Fig. 11, the relationship between highly humid layers and AOD is explored further. The maximum RH below 3 km was used as a simple parameter to quantify the presence of humid layers and the level of humidity within them for any given profile. The calculated AOD has been plotted here as a function of dry AOD ($f(\mathrm{AOD_{dry}})$) against the maximum RH for each of the 63 unsaturated RH profiles in Fig.11. The dotted line in the figure shows the calculated dry AOD ($f(\mathrm{AOD_{dry}}) = 1$) for the representative aerosol profile. This figure clearly shows an increase in wet AOD above dry in all cases. However, when layers of extremely high RH are present, this effect becomes more pronounced. When humid layers with RH higher than 95 % are present, the wet AOD is more than double the dry AOD; with layers of RH greater than 98 %, the wet AOD can be three to seven times greater than the dry. The use of $f(\mathrm{AOD_{dry}})$ allows the potential for this value to be scaled according to the dry AOD from any aerosol profile, so $\mathrm{AOD_{wet}} = f\mathrm{AOD_{dry}} \times \mathrm{AOD_{dry}}$.
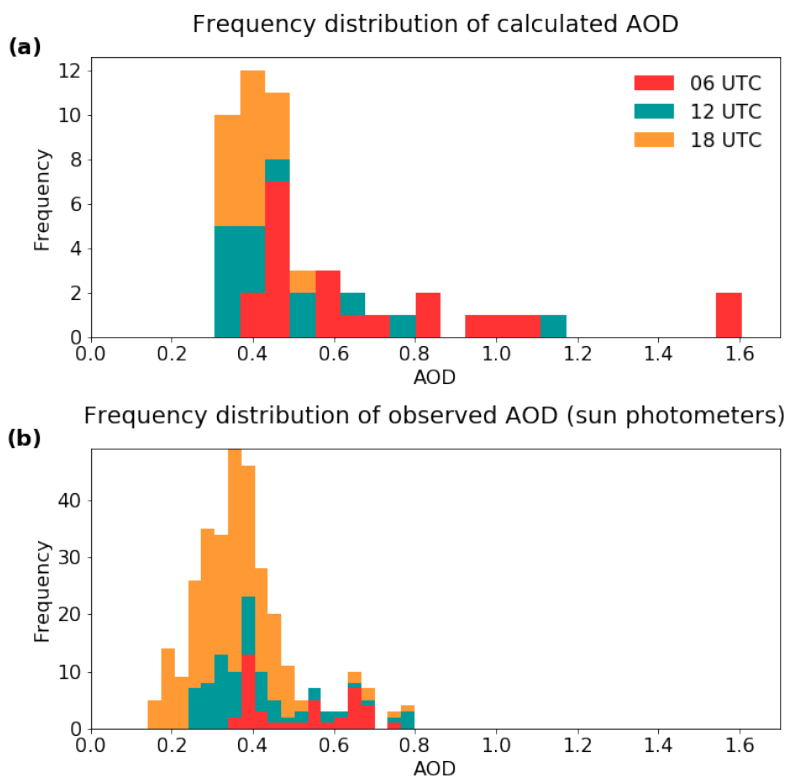
Figure 10. The frequency distributions of calculated AODs from radiosonde RHs, and AODs observed by sun photometers over Savé during the DACCIWA campaign. Values have not been calculated for 00 UTC as this is during the night.

325   A curve of best fit has been added to Fig. 11 using Igor Pro's iterative least-squares algorithm. The resulting formula can be used to calculate an estimate of the $f(\mathrm{AOD_{dry}})$ from the dry AOD and the maximum RH in the profile (Eq. 5):

$$f(AOD_{dry}) = AOD_{dry}\left[1.4 + 4.4 \times \exp\left(\frac{RH_{max} - 100}{1.4}\right)\right] \tag{5}$$

where RH is input as a value between 0 and 100. This is unlikely to be effective for values of $\mathrm{RH_{max}}$ significantly lower than those explored here. The factor of 1.4, which implies an $f(\mathrm{AOD_{dry}})$ greater than the dry AOD when RH = 0, is likely an
330   artefact created by the use of only the maximum value of RH for each RH profile. This empirical relationship could be useful for models that have no detailed treatment of aerosol chemistry.

    The frequency distribution shown in Fig. 11 shows that the RH reaches these high values a significant proportion of the time. Of the RH profiles gathered from Savé, 23 % included layers below 3 km that were unsaturated but contained layers of greater
335   than 98 % humidity. This represents 37 % of the total number of unsaturated profiles.
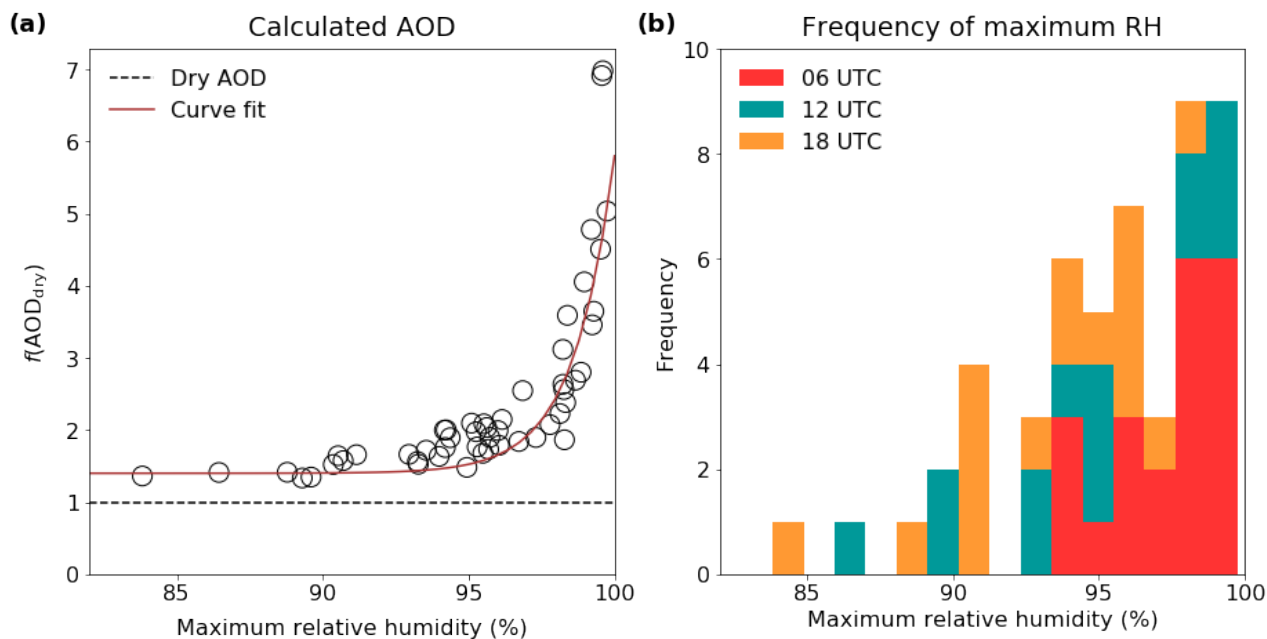
Figure 11. (a) The relationship between calculated AOD and the maximum sub-3 km RH in a profile, and **(b)** the frequency distribution of maximum unsaturated sub-3 km RH values. Bars in **(b)** are stacked.

A model-based study of aerosol liquid water content during the DACCIWA field campaign, carried out by Deetz et al. (2018a), found a mean dry AOD of 0.2 in southern West Africa, which increased to 0.7 when hygroscopic growth was taken into account. These results are highly consistent with both the dry AOD (0.22) and the calculated effect of hygroscopic growth shown here. The calculated median AOD found here was 0.46.

3.3 The effects of aerosol variability

Aerosol profiles have been assumed to be identical in all cases here. However, these loadings will in reality vary from day to day, which will have a resulting impact on the AOD. The extent of this impact can be estimated using the interquartile range of the aerosol measurements in the region, which is shown according to chemical composition in Fig. 2. At all altitudes considered here, the interquartile range of the total aerosol loading was within $0.5\,\mu g\,m^{-3}$ of $3.4\,\mu g\,m^{-3}$. This is on average around a 27 % increase or decrease in the total aerosol population in less or more polluted circumstances, which would result in a 27 % increase or decrease in the final calculated AOD. The median calculated AOD was 0.46; in this case, the less and more polluted circumstances would result in calculated AOD values of 0.34 and 0.58 respectively. This is a significant alteration in the final value.

Directly comparing this effect with that of the interquartile range of RH is complicated, due both to the strong diurnal variations in humidity and to the highly non-linear relationship between RH and the resulting HGF. However, a rough comparison of the scale of the impact of RH can be made by considering the interquartile range of the AOD data displayed in Fig. 10, which were calculated on the assumption of a constant aerosol profile. In this case, the interquartile range of the AOD is between 0.34

355   and 0.81, with a median of 0.57. This suggests that high values of RH are necessary for the highest AOD values to be produced.

The AOD scales directly with the aerosol loading. Therefore, the effects of a humid layer on a day that is more polluted than average could have an even larger effect that those shown here. The highest AOD values calculated in this study are around 1.6; this could scale to above 2 if a day is among the 25 % most polluted. As anthropogenic emissions in the region increase,

360   the number of days reaching these very high AOD values will increase. Furthermore, increased industrialisation can result in a higher proportion of inorganic, highly hygroscopic aerosol particles being produced (e.g. Morgan et al., 2009), which will exacerbate these effects.

These results suggest that the impact of highly humid layers on AOD, especially on days with high aerosol loadings, could

365   be similar to that of low-level cloud. Capturing the presence of cloud in the region using satellites and other remote sensing techniques is known to be difficult in the southern West African region; the detection of these sub-saturated humid layers adds an additional challenge. Nonetheless, it is important for their presence to be taken into account if the radiation balance in the region is to be fully understood.

4   Summary and conclusions

370   Aircraft and radiosonde data collected during the DACCIWA field campaign were used to estimate the hygroscopic growth of aerosols under different RH conditions, based on aerosol chemical composition and using the ZSR mixing rule. A consistent aerosol composition and vertical profile was assumed across the region of interest, due to the relative homogeneity of aerosol observations from the Twin Otter aircraft in the region. The RH profiles displayed a diurnal cycle, with higher RH generally observed during the night and early morning and drier conditions in the afternoon. These are features associated with the

375   Gulf of Guinea maritime inflow, described by Adler et al. (2017) and Deetz et al. (2018b), which brings cool air inland in the evening (Adler et al., in press; Babić et al., in press). Day-to-day variability was influenced by the different phases of the West African Monsoon (Knippertz et al., 2017), which resulted in slightly more frequent high RH values during the first few weeks of July.

380   By assuming a constant aerosol composition and vertical profile, it was possible to explore the effects of variations in RH on the optical properties of aerosol in the region. Dry aerosol size distributions were grown according to the HGF, which had been calculated from the RH and the average chemical composition. Mie code was then used to calculate extinction coefficients.

This allowed AODs to be calculated for each of 63 unsaturated RH profiles.

385   The median AOD resulting from these calculations was 0.46. This compares with a median AOD of 0.36 found from observations at Savè using sun photometers. The shape of the AOD frequency distribution from the calculations was comparable to that from sun photometer measurements, showing that changes in RH alone are able to account for the majority of the variability in the region's AOD.

390   The calculated dry AOD using the representative aerosol profile was 0.22. In all cases, the wet AOD was found to be at least 40 % greater than the AOD for dry particles, showing the substantial impact of hygroscopic growth on optical properties. The rate of change of AOD with changes in RH was greater at higher RH. In particular, at values of RH greater than 98 %, the wet AOD was five to seven times larger than the dry AOD. This scenario ocurred regularly in the field RH measurements, with 37 % of unsaturated profiles featuring a humid layer of at least 98 % RH. These results are consistent with model results

395 presented by Deetz et al. (2018a), who found that hygroscopic growth increased the AOD in the southern West African region from a dry value of 0.2 to a wet value of 0.7.

    While aerosol loadings were assumed here to be constant, aircraft measurements in fact showed an interquartile range of ±27 %. Taking this variation into account would result in the average AOD varying between 0.34 and 0.58. It is important

400 to note that the increase in AOD due to an increase in aerosol loading is linear, while that resulting from an increase in RH is exponential. Thus, the presence of highly humid layers in the column will substantially enhance any effect from increased aerosol loading. The highest AOD values would not be possible without this RH enhancement.

    These results show that the presence of highly humid layers during the monsoon season has a substantial impact on the direct

405 radiative effect of aerosols in the southern West African region. Furthermore, as anthropogenic emissions from large cities in coastal West Africa increase and industrialisation increases the inorganic fraction, these humid layers will serve to amplify their effects. While detecting these layers and quantifying their effects on an ongoing basis is likely to provide a significant challenge for the research community, results shown here suggest that this will be necessary if the radiation balance in the region is to be understood.

410 *Data availability.*   The underlying research data are available upon request from the corresponding author.

    Competing interests. The authors declare that they have no conflict of interest.

    Special issue statement. This article is part of the special issue *Results of the project "Dynamics–aerosol–chemistry–cloud*

415 *interactions in West Africa" (DACCIWA)*

Acknowledgements. The research leading to these results has received funding from the European Union 7th Framework Programme (FP7/2007-2013) under Grant Agreement no. 603502 (EU project DACCIWA: Dynamics-aerosol-chemistry-cloud interactions in West Africa). The lead author was supported by the NERC Doctoral Training Programme (grant ref: NE/L002469/1). Thanks to the German Weather Service (DWD) for providing access to the ICON forecast data.

References

Adler, B., Kalthoff, N., and Gantner, L.: Nocturnal low-level clouds over southern West Africa analysed using high-resolution simulations, Atmos. Chem. Phys., 17, 899–910, https://doi.org/10.5194/acp-17-899-2017, 2017.

Adler, B., Babić, K., Kalthoff, K., Lohour, F., Lothon, M., Dione, C., Pedruzo-Bagazgoitia, X., and Andersen, H.: Nocturnal low-level clouds in the atmospheric boundary layer over Southern West Africa: an observation-based analysis of conditions and processes, Atmos. Chem. Phys. Discuss., in press.

Aklilu, Y., Mozurkewich, M., Prenni, A. J., Kreidenweis, S. M., Alfarra, M. R., Allan, J. D., Anlauf, K., Brooks, J., Leaitch, W. R., Sharma, S., Boudries, H., and Worsnop, D. R.: Hygroscopicity of particles at two rural, urban influenced sites during Pacific 2001: Comparison with estimates of water uptake from particle composition, Atmos. Environ., 40, 2650–2661, https://doi.org/10.1016/j.atmosenv.2005.11.063, 2006.

Babić, K., Adler, B., Kalthoff, N., Andersen, H., Dione, C., Lohou, F., Lothon, M., and Pedruzo-Bagazgoitia, X.: The observed diurnal cycle of nocturnal low-level stratus clouds over southern West Africa: a case study, Atmos. Chem. Phys. Discuss., in press.

Bond, T. C. and Bergstrom, R. W.: Light Absorption by Carbonaceous Particles: An Investigative Review, Aerosol Sci. Technol., 40, 27–67, https://doi.org/10.1080/02786820500421521, http://www.tandfonline.com/doi/abs/10.1080/02786820500421521, 2006.

Boucher, O., Randall, D., Artaxo, P., Bretherton, C., Feingold, G., Forster, P., Kerminen, V.-M., Kondo, Y., Liao, H., Lohmann, U., Rasch, P., Satheesh, S. K., Sherwood, S., Stevesn, B., and Zhang, X. Y.: Clouds and aerosols, in: Clim. Chang. 2013 Phys. Sci. Basis. Contrib. Work. Gr. I to Fifth Assess. Rep. Intergov. Panel Clim. Chang., edited by Stocker, T. F., Qin, D., Plattner, G.-K., Tignor, M., Allen, S. K., Boschung, J., Nauels, A., Xia, Y., Bex, V., and Midgley, P. M., chap. 7, pp. 571–657, Cambridge University Press, Cambridge, United Kingdom and New York, NY, USA, http://www.ipcc.ch/pdf/assessment-report/ar5/wg1/WG1AR5{_}Chapter07{_}FINAL.pdf, 2013.

Brito, J., Freney, E., Dominutti, P., Borbon, A., Haslett, S. L., Batenburg, A. M., Colomb, A., Dupuy, R., Denjean, C., Burnet, F., Bourriane, T., Deroubaix, A., Sellegri, K., Borrmann, S., Coe, H., Flamant, C., Knippertz, P., and Schwarzenboeck, A.: Assessing the role of anthropogenic and biogenic sources on PM_1 over southern West Africa using aircraft measurements, Atmos. Chem. Phys., pp. 757–772, https://doi.org/10.5194/acp-18-757-2018, 2018.

Canagaratna, M., Jayne, J., Jimenez, J., Allan, J., Alfarra, M., Zhang, Q., Onasch, T., Drewnick, F., Coe, H., Middlebrook, A., Delia, A., Williams, L., Trimborn, A., Northway, M., DeCarlo, P., Kolb, C., Davidovits, P., and Worsnop, D.: Chemical and microphysical characterization of ambient aerosols with the aerodyne aerosol mass spectrometer, Mass Spectrometry Reviews, 26, 185–222, https://doi.org/10.1002/mas.20115, http://dx.doi.org/10.1002/mas.20115, 2007.

Chen, J., Zhao, C. S., Ma, N., Liu, P. F., Göbel, T., Hallbauer, E., Deng, Z. Z., Ran, L., Xu, W. Y., Liang, Z., Liu, H. J., Yan, P., Zhou, X. J., and Wiedensohler, A.: A parameterization of low visibilities for hazy days in the North China Plain, Atmos. Chem. Phys., 12, 4935–4950, https://doi.org/10.5194/acp-12-4935-2012, 2012.

Deetz, K., Vogel, H., Haslett, S., Knippertz, P., Coe, H., and Vogel, B.: Aerosol liquid water content in the moist southern West African monsoon layer and its radiative impact, Atmos. Chem. Phys. Discuss., https://doi.org/10.5194/acp-2018-420, 2018a.

Deetz, K., Vogel, H., Knippertz, P., Adler, B., Taylor, J., Coe, H., Bower, K., Haslett, S., Flynn, M., Dorsey, J., Crawford, I., Kottmeier, C., and Vogel, B.: Cloud and aerosol radiative effects as key players for anthropogenic changes in atmospheric dynamics over southern West Africa, Atmos. Chem. Phys. Discuss., https://doi.org/10.5194/acp-2018-186, 2018b.

455   Drewnick, F., Hings, S. S., DeCarlo, P., Jayne, J. T., Gonin, M., Fuhrer, K., Weimer, S., Jimenez, J. L., Demerjian, K. L., Borrmann, S.,
        and Worsnopp, D. R.: A new time-of-flight Aerosol Mass Spectrometer (TOF-AMS) - instrument description and first field deployment,
        Aerosol Sci. Technol., 39, 637–658, https://doi.org/10.1080/02786820500182040, 2005.

        Esteve, A. R., Highwood, E. J., Morgan, W. T., Allen, G., Coe, H., Grainger, R. G., Brown, P., and Szpek, K.: A study on the sensitivities
        of simulated aerosol optical properties to composition and size distribution using airborne measurements, Atmos. Environ., 89, 517–524,
460   https://doi.org/10.1016/j.atmosenv.2014.02.063, 2014.

        Flamant, C., Knippertz, P., Fink, A., Akpo, A., Brooks, B., Chiu, C., Coe, H., Danuor, S., Evans, M., Jegede, O., Kalthoff, N., Konaré, A.,
        Liousse, C., Lohou, F., Mari, C., Schlager, H., Schwarzenboeck, A., Adler, B., Amekudzi, L., Aeyee, J., Ayoola, M., Bessardon, G., Bower,
        K., Burnet, F., Catoir, V., Colomb, A., Fossu-Amankwah, K., Lee, J., Lothon, M., Manaran, M., Marsham, J., Meynadier, R., Ngamini, J.-
        B., Rosenberg, P., Sauer, D., Schneider, J., Smith, V., Stratmann, G., Voigt, C., and Yoboue, V.: The Dynamics-Aerosol-Chemistry-Cloud
465   Interactions in West Africa field campaigns: Overview and research highlights, Bull. Amer. Meteor. Soc., https://doi.org/10.1175/BAMS-
        D-16-0256.1, 2018a.

        Forster, P., Ramaswamy, V., Artaxo, P., Berntsen, T., Betts, R., Fahey, D. W., Haywood, J., Lean, J., Lowe, D. C., Myhre, G., Nganga, J.,
        Prinn, R., Raga, G., Schulz, M., and Dorland, R. V.: Changes in atmospheric constituents and in radiative forcing, chap. 2, Cambridge
        University Press, Cambridge, United Kingdom and New York, NY, USA, 2007.

470   Gysel, M., Crosier, J., Topping, D. O., Whitehead, J. D., Bower, K. N., Cubison, M. J, ., Williams, P. I., Flynn, M. J., McFiggans, G. B.,
        and Coe, H.: Closure study between chemical composition and hygroscopic growth of aerosol particles during TORCH2, Atmos. Chem.
        Phys., 7, 6131–3144, https://doi.org/10.5194/acp-7-6131-2007, 2007.

        Hannak, L., Knippertz, P., Fink, A. H., Kniffka, A., and Pante, G.: Why do global climate models struggle to represent low-level clouds in
        the West African summer monsoon?, J. Climate, 30, 1665–1687, https://doi.org/10.1175/JCLI-D-16-0451.1, 2017.

475   Hersey, S. P., Sorooshian, A., Murphy, S. M., flagan, R. C., and Seinfeld, J. H.: Aerosol hygroscopicity in the marine atmosphere: a clo-
        sure study using high-time-resolution, multiple-RH DASH-SP and size-resolved C-ToF-AMS data, Atmos. Chem. Phys., 9, 2543–2554,
        https://doi.org/10.5194/acp-9-2543-2009, 2009.

        Highwood, E. J., Northway, M. J., Mcmeeking, G. R., Morgan, W. T., Liu, D., Osborne, S., Bower, K., Coe, H., Ryder, C., and Williams,
        P.: Aerosol scattering and absorption during the EUCAARI-LONGREX flihts of the Facility for Airborne Atmospheric Measurements
480   (FAAM) BAe-146: can measurements and models agree?, Atmos. Chem. Phys., 12, 7251–7267, https://doi.org/10.5194/acp-12-7251-
        2012, 2012.

        Juránýi, Z., Weingartner, E., DeCarlo, P. F., Kammermann, L., and Baltensperger, U.: Measured and modelled cloud condensation nuclei
        number concentration at the high alpine site Jungfraujoch, Atmos. Chem. Phys., 10, 7891–7906, https://doi.org/10.5194/acp-10-7891-
        2010, 2010.

485   Kalthoff, N., Lohou, F., Brooks, B., Jegede, G., Adler, B., Babić, K., Dione, C., Ajao, A., Amekudzi, L. K., Aryee, J. N. A., Ayoola, M.,
        Bessardon, G., Danuor, S. K., Handwerker, J., Kohler, M., Lothon, M., Pedruzo-Bagazgoitia, X., Smith, V., Sunmonu, L., Wieser, A., Fink,
        A. H., and Knippertz, P.: An overview of the diurnal cycle of the atmospheric boundary layer during the West African monsoon season:
        Results from the 2016 observational campaign, Atmos. Chem. Phys., 18, 2913–2928, https://doi.org/10.5194/acp-2017-631, 2018.

        Kamilli, K. A., Poulain, L., Held, A., Nowak, A., Birmili, W., Wiedensohler, A., and Kamilli, K.: Hygroscopic properties of the Paris urban
490   aerosol in relation to its chemical composition, Atmos. Chem. Phys., 14, 737–749, https://doi.org/10.5194/acp-14-737-2014, 2014.

Knippertz, P., Coe, H., Chiu, J. C., Evans, M. J., Fink, A. H., Kalthoff, N., Liousse, C., Mari, C., Allan, R. P., Brooks, B., Danour, S., Flamant, C., Jegede, O. O., Lohou, F., and Marsham, J. H.: The DACCIWA Project: Dynamics–Aerosol–Chemistry–Cloud Interactions in West Africa, Bull. Am. Meteorol. Soc., 96, 1451–1460, https://doi.org/10.1175/BAMS-D-14-00108.1, 2015.

Knippertz, P., Find, A. H., Deroubaix, A., Morris, E., Tocquer, F., Evans, M. J., Flamant, C., Gaetani, M., Lavaysse, C., Mari, C., Marsham, J. H., Meynadier, R., Affo-Dogo, A., Bahaga, T., Brosse, F., Deetz, K., Guebsi, R., Latifou, I., Maranam, M., Rosenberg, P. D., and Schlueter, A.: A meteorological and chemical overview of the DACCIWA field campaign in West Africa in June–July 2016, Atmos. Chem. Phys., 17, 10 893–10 918, https://doi.org/10.5194/acp-17-10893-2017, 2017.

Laborde, M., Schnaiter, M., Linke, C., Saathoff, H., Naumann, K.-H., Möhler, O., Berlenz, S., Wagner, U., Taylor, J. W., Liu, D., Flynn, M., Allan, J. D., Coe, H., Heimerl, K., Dahlkötter, F., Weinzierl, B., Wollny, A. G., Zanatta, M., Cozic, J., Laj, P., Hitzenberger, R., Schwarz, J. P., and Gysel, M.: Single Particle Soot Photometer intercomparison at the AIDA chamber, Atmos. Meas. Tech., 5, 3077–3097, https://doi.org/10.5194/amt-5-3077-2012, 2012.

Liousse, C., Assamoi, E., Criqui, P., Granier, C., and Rosset, R.: Explosive growth in African combustion emissions from 2005 to 2030, Environ. Res. Lett., 9, 035 003, https://doi.org/10.1088/1748-9326/9/3/035003, 2014.

Liu, H. J., Zhao, C. S., Nekat, B., Ma, N., Wiedensohler, A., Van Pinxteren, D., Spindler, G., Müller, K., and Herrmann, H.: Aerosol hygroscopicity derived from size-segregated chemical composition and its parameterization in the North China Plain, Atmos. Chem. Phys., 14, 2525–2539, https://doi.org/10.5194/acp-14-2525-2014, 2014.

Liu, P. F., Zhao, C. S., Göbel, T., Hallbauer, E., Nowak, A., Ran, L., Xu, W. Y., Deng, Z. Z., Ma, N., Mildenberger, K., Henning, S., Stratmann, F., and Wiedensohler, A.: Hygroscopic properties of aerosol particles at high relative humidity and their diurnal variations in the North China Plain, Atmos. Chem. Phys., 11, 3479–3494, https://doi.org/10.5194/acp-14-2525-2014, 2011.

Lowenthal, D. H., Kumar, N., Hand, J., Day, D., Kreidenweis, S., Collett, J., Lee, T., and Ashbaugh, L.: Journal of the Air & Waste Management Association Hygroscopic Organic Aerosols during BRAVO? Hygroscopic Organic Aerosols during BRAVO?, J. Air Waste Manage. Assoc., 53, 1273–1279, https://doi.org/10.1080/10473289.2003.10466284, http://www.tandfonline.com/action/journalInformation?journalCode=uawm20https://doi.org/10.1080/10473289.2003.10466284, 2003.

McFiggans, G., Alfarra, M. R., Allan, J., Bower, K., Coe, H., Cubison, M., Topping, D., Williams, P., Decesari, S., Facchini, C., and Fuzzi, S.: Simplification of the representation of the organic component of atmospheric particulates, Faraday Discuss., 130, 341, https://doi.org/10.1039/b419435g, 2005.

Middlebrook, A. M., Bahreini, R., Jimenez, J. L., and Canagaratna, M. R.: Evaluation of composition-dependent collection efficiencies for the Aerodyne Aerosol Mass Spectrometer using field data, Aerosol Sci. Technol., 46, 257–271, https://doi.org/10.1080/02786826.2011.62004, 2011.

Morgan, W. T., Allan, J. D., Bower, K. N., Capes, G., Crosier, J., Williams, P. I., and Coe, H.: Vertical distribution of submicron aerosol chemical composition from North-Western Europe and the North-East Atlantic, Atmos. Chem. Phys., 9, 5389–5401, https://doi.org/10.5194/acp-9-5389-2009, 2009.

Morgan, W. T., Allan, J. D., Bower, K. N., Esselborn, M., Harris, B., Henzing, J. S., Highwood, E. J., Kiendler-Scharr, A., McMeeking, G. R., Mensah, A. A., Northway, M. J., Osborne, S., Williams, P. I., Krejci, R., and Coe, H.: Enhancement of the aerosol direct radiative effect by semi-volatile aerosol components: airborne measurements in North-Western Europe, Atmos. Chem. Phys., 10, 8151–8171, https://doi.org/10.5194/acp-10-8151-2010, 2010.

Penner, J. E., Chuang, C. C., and Grant, K.: Climate forcing by carbonaceous and sulfate aerosols, Clim. Dyn., 14, 839–851, https://doi.org/10.1007/s003820050259, http://link.springer.com/10.1007/s003820050259, 1998.

Petters, M. D. and Kreidenweis, S. M.: A single parameter representation of hygroscopic growth and cloud condensation nucleus activity, Atmos. Chem. Phys., 7, 1961–1971, https://doi.org/10.5194/acp-7-1961-2007, 2007.

Pratt, K. A. and Prather, K. A.: Aircraft measurements of vertical profiles of aerosol mixing states, J. Geophys. Res., 115, D11 305, https://doi.org/10.1029/2009JD013150, 2010.

Pringle, K. J., Tost, H., Pozzer, A., Pöschl, U., and Lelieveld, J.: Global distribution of the effective aerosol hygroscopicity parameter for CCN activation, Atmos. Chem. Phys., 10, 5241–5255, https://doi.org/10.5194/acp-10-5241-2010, 2010.

Stelson, A. W.: Urban aerosol refractive-index prediction by partial molar refraction approach, Environ. Sci. Technol., pp. 1676–1679, https://doi.org/10.1021/es00081a008, 1990.

Stokes, R. H. and Robinson, R. A.: Interactions in aqueous nonelectrolyte solutions. I. Solute-solvent equilibria, J. Phys. Chem., 70, 2126–2130, https://doi.org/10.1021/j100879a010, 1966.

Suda, S. R., Petters, M. D., Matsunaga, A., Sullivan, R. C., Ziemann, P. J., and Kreidenweis, S. M.: Hygroscopicity frequency distributions of secondary organic aerosols, Journal of Geophysical Research: Atmospheres, 117, n/a–n/a, https://doi.org/10.1029/2011JD016823, http://dx.doi.org/10.1029/2011JD016823, d04207, 2012.

Swietlicki, E., Hansson, H.-C., Hämeri, K., Svenningsson, B., Massling, A., McFiggans, G., McMurry, P. H., Petäjä, T., Tunved, P., Gysel, M., Topping, D., Weingartner, E., Baltensperger, U., Rissler, J., Wiedensohler, A., and Kulmala, M.: Hygroscopic properties of submicrometer atmospheric aerosol particles measured with H-TDMA instruments in various environments - a review, Tellus B, 60, 432–469, https://doi.org/10.1111/j.1600-0889.2008.00350.x, 2008.

Taylor, J. W., Allan, J. D., Liu, D., Flyn, M., Weber, R., Zhang, X., Lefer, B. L., Grossberg, N., Flynn, J., and Coe, H.: Assessment of the sensitivity of core / shell parameters derived using the single-particle soot photometer to density and refractive index, Atmos. Meas. Tech., pp. 1701–1718, https://doi.org/10.5194/amt-8-1701-2015, 2015.

Toon, O. B., Pollack, J. B., and Khare, B. N.: The optical constants of several atmospheric aerosol species: Ammonium sulfate, aluminum oxide, and sodium chloride, J. Geophys. Res., 81, 5733–5748, https://doi.org/10.1029/JC081i033p05733, http://doi.wiley.com/10.1029/JC081i033p05733, 1976.

Topping, D. O., McFiggans, G. B., and Coe, H.: A curved multi-component aerosol hygroscopicity model framework: part 2 - including organic compounds, Atmos. Chem. Phys., 5, 1223–1242, https://doi.org/10.5194/acp-5-1223-2005, 2005.

Weast, R. C.: Handbook of Chemistry and Physics, CRC Press, Florida, 66 edn., 1985.

Weingartner, E., Burtscher, H., and Baltensperger, U.: Hygroscopic properties of carbon and diesel soot particles, Atmos. Environ., 31, 2311–2327, https://doi.org/10.1016/S1352-2310(97)00023-X, 1997.

Yang, W.: Improved recursive algorithm for light scattering by a multilayered sphere, Appl. Opt., 42, 1710–1720, https://doi.org/10.1364/AO.42.001710, 2003.

Zdanovskii, A. B.: New methods for calculation solubilities of electrolytes in multicomponent systems, Zhur. Fiz. Kim., 22, 1475–1485, 1948.